



# Confinement of air in the Asian monsoon anticyclone and pathways of convective air to the stratosphere during summer season

Bernard Legras and Silvia Bucci

Laboratoire de Météorologie Dynamique, UMR 8539, CNRS/PSL-ENS/Sorbonne Université/Ecole Polytechnique, Paris, France

**Correspondence:** Bernard Legras (bernard.legras@lmd.ens.fr)

**Abstract.** We study the transport pathways from the top of convective clouds to the lower tropical stratosphere during the Asian monsoon, using massive Lagrangian trajectories driven by observed clouds and the two reanalysis ERA-Interim and ERA5 with diabatic and kinematic vertical motions. We find that the upward propagation of convective impact is very similar for the kinematic and diabatic calculations using ERA5 while the two cases strongly differ for ERA-Interim. The separation of descending and ascending motion occurs at a crossover level which is slightly above the all sky zero level of radiative heating rate, except over the Tibetan plateau. The parcels that stay confined within the Asian monsoon anticyclone and reach 380 K are mostly of continental origin while maritime sources are dominating when the whole global 380 K surface is considered. We find that the strong impact of the Tibetan plateau with respect to its share of high clouds is entirely due to its elevated proportion of high clouds above the crossover. We find no trace of a vertical conduit above convection over the Tibetan plateau; parcels are rather entrained into an ascending spiral motion that spans the whole anticyclone. The mean age of parcels with respect to convection exhibits a minimum at the centre of the Asian monsoon anticyclone due to the permanent renewal by fresh convective air and largest values on the periphery as air spirals out. The contrast is reduced by dilution for increasing potential temperature. We find that the confinement above 360 K can be represented, on the average, by a simple 1D process of diabatic advection with loss. The mean loss time is about 13 days and uniform over the range 360 K to 420 K which is to be compared with a total circulation time of two to three weeks around the anticyclone. The vertical dilution is consequently exponential with an e-folding potential temperature scale of 15 K (about 3 km).

## 1 Introduction

The Asian monsoon is the most active convective region during boreal summer and, as such, is also the largest provider of air ascending from the tropospheric boundary layer to the upper troposphere and the lower stratosphere. Usually the air does not ascend directly into the stratosphere but convective air is mostly detrained below the tropopause within the tropical tropopause layer (TTL) and is subsequently carried aloft by slow motion (Fueglistaler et al., 2009). The bulk of the convective detrainment occurs at about 200 hPa or 350 K (12-13 km) and is associated with the divergent upper component of the Hadley circulation (Garny and Randel, 2013). At such altitudes the vertical motion is almost everywhere descending except within the clouds, due to a dominating radiative cooling. It is only at about 355-360 K (14-15km), depending on the location, that the mean clear



sky radiative cooling leaves room to warming (McFarlane et al., 2007). As the short wave absorption is very small at such levels, this is mainly a long wave effect which is due to the very cold temperature at the tropopause, such that the absorption of upward long-wave radiation exceeds the emission. This cold temperature is maintained by the adiabatic cooling of the air pumped across the tropopause and entering the Brewer-Dobson circulation (Randel et al., 2007; Randel and Jensen, 2013).

5 The radiative effect of clouds in their environment provides a cooling or warming perturbation that can, accordingly, rise or lower locally the mean all sky level of zero radiative heating (LZRH) (Yang et al., 2010; Wright and Fueglistaler, 2013; Berry and Mace, 2014; Johansson et al., 2015). As this LZRH plays the role of a repelling barrier, a question is whether it forbids air parcels detrained below to reach levels above. It was proposed (Corti et al., 2006) that the radiative heating provided by cirrus clouds may help parcel to cross the LZRH. However, Tissier and Legras (2016) found that this seldom happens and that

10 convective sources of air reaching the tropopause are for 80% located above the LZRH.

During the Asian monsoon, a wide anticyclonic circulation denoted as the Asian Monsoon Anticyclone (AMA) sits over the lower layer quasi-stationary low pressure centre. This circulation, which reaches its maximum intensity near 360 K, ventilates the top of the monsoon convective clouds and redistributes the detrained air over a large area. Satellite observations show that tropospheric compounds emitted at the surface, like CO, and aerosols generated from these compounds, tend to concentrate

15 within the AMA while it is depleted in stratospheric borne ozone (Randel and Park, 2006; Park et al., 2008; Randel et al., 2010; Vernier et al., 2015; Santee et al., 2017; Luo et al., 2018). These observations have been corroborated by a number of numerical simulations based on Lagrangian or general circulation models which all show confinement of tropospheric tracers within the AMA (James et al., 2008; Park et al., 2009; Tzella and Legras, 2011; Wright et al., 2011; Bergman et al., 2012, 2013; Orbe et al., 2015; Vogel et al., 2015; Yan and Bian, 2015; Tissier and Legras, 2016; Garny and Randel, 2016; Pan et al., 2016; Fan et al., 2017; Ploeger et al., 2017; Vogel et al., 2019). There is, however, a dispersion in the interpretation of what is actually

20 observed. Basically, some studies support that the ascent of air within the AMA, in the clouds and above the clouds, canalize the flow from the troposphere to the stratosphere in a sort of chimney with a core above the Tibetan plateau. This upward flow would be then redistributed horizontally at the top of the chimney, corresponding approximately to the tropopause level above the Tibetan plateau (Bergman et al., 2013; Pan et al., 2016; Ploeger et al., 2017). Other studies see a broader spiralling

25 ascent and stress that only a limited part of the ascending flux is processed within the AMA and that a large flux, mostly of maritime origin, finds its way to the stratosphere by circulating around the AMA but without penetrating its core (Orbe et al., 2015; Tissier and Legras, 2016; Fan et al., 2017; Vogel et al., 2019). It has been discussed that some of these discrepancies can be due to the differences between the reanalyzed winds, vertical velocities and heating rates which are quite different among available reanalysis, being notoriously large between ERA-Interim/IFS and MERRA-2/GEOS5, the most used by modellers,

30 in the Asian monsoon region (Tegtmeier et al., 2019b).

The goal of this work is to seize the opportunity of the release of the ERA5 by the European Centre of Medium Range Weather Forecast (ECMWF), a new generation reanalysis incorporating very recent progresses in numerical weather forecast, to revisit this problem in a systematic and quantitative way. In addition, we use state of the art diagnostics of the heights of convective clouds from high frequency and high resolution geostationary observations. We also focus on reconciling previous



studies by providing a simple quantitative account of the modelled transport across the TTL with a 1D model of transport with losses.

Section 2 describes the data and methods used in this study. Section 3 presents the results of the extensive 3D Lagrangian calculations. Section 4 discusses how a simple 1D model can reproduce the properties of the 3D transport across the TTL.

5 Section 5 offers discussion and conclusion. Complementary results and discussions can be found in the Supplement.

## 2 Data and methods

### 2.1 ECMWF reanalysis

We compare here the two reanalysis ERA-Interim and ERA5 of the ECMWF. The ERA-Interim was initially made available at the end of 2007. It is based on the Cy31r2 version of the Integrated Forecast System (IFS), released in 2006, with T255L  
10 spectral resolution and 60 hybrid levels up to 0.1 hPa (Dee et al., 2011). It uses a 4D-Var assimilation with a 12h cycle. The ERA5 reanalysis (Copernicus Climate Change Service, C3S, 2017) was initially made available at the end of 2017. It is based on the C41r2 version of the IFS model with T1367 spectral resolution and 137 hybrid levels up to 0.01 hPa. It uses an ensemble 4D-Var assimilation with a 12h cycle. Between 155 and 65 hPa, the number of hybrid levels has changed from 6 to 17, providing much better vertical resolution in the region of the atmosphere relevant to this study. The IFS has undergone  
15 many changes between ERA-Interim and ERA5, in particular regarding the parametrization of cloud processes.

We use ERA-Interim winds, temperature and diabatic heating rates on the hybrid levels of the model at a 1° horizontal resolution in latitude and longitude over the sphere. Winds are available from both the analysis and the forecast while heating rates are a pure forecast product. The data are available 3-hourly by interspelling 3h and 9h forecasts with the analysis available every 6h

20 We use ERA5 winds, temperature and diabatic heating rates on the hybrid levels of the model at a 0.25° horizontal resolution in latitude and longitude within the FullAMA domain bounded by 10°W and 160°E in longitude and 0 and 50°N in latitude. See more details about this choice in Sect. 2.3. The data are available hourly from analysis (winds and temperature) and forecasts (heating rates). Notice that in both ERA-Interim and ERA-5, the winds and temperature are available as instantaneous fields while the radiative heating are, respectively, 3-hourly and hourly accumulations.

25 Significant differences in the cloud properties over the Asian monsoon region are visible between ERA-Interim and ERA5 as documented in Tegtmeier et al. (2019b). The maximum cloud cover occurs at a lower level in the ERA-Interim than in the ERA5 and is smaller. The ERA5, however, exhibits more high penetrative convection than the ERA-Interim, especially over the Tibetan plateau (Tegtmeier et al., 2019b) and more activity at better resolved small scales in general (Hoffmann et al., 2019). Fig.1 shows the resulting cloud radiative heating (CRH) in the monsoon region for both reanalysis. The CRH is located  
30 lower in altitude for ERA5 and therefore disturbs the clear sky LZRH on a less extended region than for the ERA-Interim. It can be shown that the ERA5 disturbance of the LZRH concentrates over land and in particular over the Tibetan plateau which corresponds to the largest lobe in the green curve. On the overall the ERA5 heating rate are the more consistent with estimates



based on active satellite measurements of the cloud vertical distribution (Berry and Mace, 2014; Johansson et al., 2015) as shown in Tegtmeier et al. (2019b) when compared with four other reanalysis.

## 2.2 Lagrangian trajectories

Lagrangian trajectories are calculated using the Lagrangian model TRACZILLA (Pisso and Legras, 2008), which is a variation of FLEXPART (Stohl et al., 2005). TRACZILLA interpolates velocities and heating rate directly from the hybrid grid to the location of the parcel using log pressure interpolation or potential temperature interpolation in the vertical. The nominal vertical coordinate can be log pressure for kinematic calculations using vertical velocities or potential temperature for diabatic calculations using radiative heating rates. The time step is 7.5 minutes. In both cases, temperature and pressure are calculated along the trajectory. As the trajectories are intended to wander outside of clouds, the diabatic calculation use the total radiative heating rate but discard the latent heating as well as the vertical heat diffusion, the latter being generally negligible in the region of interest. The kinematic calculations use the total vertical velocity that includes the net convective flux, that cannot be separated. This set-up is quite similar to that of, e.g., Bergman et al. (2013). Some other studies where the tracers are initialized in the boundary layer used instead the total heating rate (Vogel et al., 2015; Ploeger et al., 2017; Vogel et al., 2019; Li et al., 2019). Above the level of maximum cloud cover, the total heating rate converges rapidly to the radiative heating rate as a function of increasing potential temperature.

## 2.3 Domain

Observations show that there is a strong correlation in averaged maps between the geopotential or Montgomery potential contours and tracer contours (Park et al., 2007, 2009), showing the confinement properties of the AMA. The mean Montgomery potential for several levels during Summer 2017 is shown in Fig. S2 of the Supplement. However, the AMA fluctuates a lot from day to day and it is much more difficult to define an operational boundary on instantaneous maps. Ploeger et al. (2015) use the gradient of potential vorticity to mark the boundary of the AMA but very often this boundary is fuzzy with numerous patches. We avoid this problem by considering a domain, denoted as FullAMA, that is intended to encompass the AMA and reveals its confinement properties but, at the same time, to be small enough such that trajectories leaving the AMA also leave the domain very shortly after. The FullAMA domain is bounded in longitude by 10°W and 160°E and in latitude by 0°N and 50°N. This choice is also dictated by practical considerations as it is very costly to manage calculations using the ERA5 at full resolution in the global domain.

Therefore, the ERA5 calculations are conducted within the FullAMA domain, all trajectories reaching its boundary being discarded while the ERA-Interim calculations are conducted both in the global domain and the FullAMA domain (the latter configuration being obtained by clipping the global trajectories who leaves FullAMA) for the sake of comparison. In addition, all trajectories reaching the 30 hPa or 500 hPa surfaces are discarded since parcels then exit the vertical region of interest. The global calculations of the ERA-Interim are also exploited to study the impact of the monsoon at planetary scale.



A second restricted domain, the AMACore, is defined to fit the region of closed streamlines in the Montgomery potential shown in Fig. S2. This domain is bound by  $10^{\circ}\text{E}$  and  $140^{\circ}\text{E}$  in longitude and by  $10^{\circ}\text{N}$  and  $40^{\circ}\text{N}$  in latitude. It spans the core of the AMA circulation.

## 2.4 Cloud data and trajectory sources

5 We characterize cloud tops using the SAF-NWC (Eumetsat Satellite Application Facility for Nowcasting) software package (Derrien and Le Gléau, 2010; Sèze et al., 2015) that determines cloud type and cloud top height from geostationary satellites using visible and infra-red channels. The 2016 version of the SAF-NWC package has been applied to the MSG1 (Meteosat 8) and Himawari satellites at full spatial resolution with  $15'$  sampling for MSG1 and  $20'$  sampling for Himawari during June-July-August 2017. MSG1 is used west of  $90^{\circ}\text{E}$  and Himawari east of this longitude. The auxiliary temperature profiles are provided  
10 from the ERA5 at hourly temporal resolution and 32 pressure levels, as well as the altitude and the temperature of the thermal tropopause. The cloud data are projected onto a regular grid in the AMA domain with spatial resolution  $0.1^{\circ}$  in both longitude and latitude using the closest neighbour method. The data on this grid are updated every 5 minutes to the most recent satellite data. When a satellite image is missing, the gap is filled by the last one available for this satellite. The SAF-NWC package uses an ensemble of retrieval algorithms choosing the best one for each pixel according to a selection tree. See Bucci et al.  
15 (2019) for a more detailed account of the algorithm. Depending on the retrieval path, the cloud top pressure can be determined among a continuous range or within a set of discrete values. In particular, a small number of single pixel cloud tops are found at 100 and 70 hPa. We have not filtered these values as they are found at the core of very high and cold systems and are liable to capture overshooting events. No convective clouds are considered outside of the FullAMA domain.

In forward runs, cloud tops are used to initialize trajectories every hour by selecting high clouds in the FullAMA domain at  
20 that time: we retain all clouds above 250 hPa within high and very high opaque and thick semi-transparent types as per the SAF-NWC classification. For each of these cloud pixels, a new trajectory is launched at its top and is integrated forward in time for up to 2 months. Notice that a large number of mid-level clouds which are associated with heavy monsoon precipitations escape this selection.

Parcels are launched hourly from the top of the clouds over the period June-August 2017. On the overall 308 millions  
25 trajectories have been launched during this period. Four separate integrations are performed. The first two uses the ERA5 dataset and are bounded within the FullAMA domain. In the sequel, the diabatic version is labelled EAD and the kinematic version is labeled EAZ The last two integrations are performed using the ERA-Interim dataset and the trajectories are integrated within the global domain. The diabatic version is labelled EID and the kinematic version is labelled EIZ.

In backward runs, the trajectories are initiated on a one degree grid at selected potential temperature and are launched every  
30 15 minutes in the FullAMA domain, and every hour in the global domain for July-August-September 2017. The trajectories are integrated backward for up to two months when they do not exit the domain. The trajectories are processed to find encounters with clouds. This is done, for each parcel, from 6-hourly outputs by interpolating the parcel position every 5 minutes and comparing the parcel pressure with that of the cloud tops from the SAF-NWC image which is valid at that time (and renewed every  $15'$  or  $20'$ ). When a cloud top with lower pressure than the parcel is found at the same location, the backward trajectory



is flagged as ending there. Due to flaws in the retrieval, 24 images have been blacklisted during Summer 2017 and removed from the processing.

## 2.5 Convective impact

The effect of the transport of monsoon convective parcels in forward calculations is measured as the convective impact. Basically, we divide the tropical atmosphere into cells of width  $D = 1^\circ$  in latitude-longitude and of height  $\Delta\theta = 5$  K. We then count the number of convective parcels found within this cell over the full two months of integration. This count can be performed in the *target space*, that is at the location of the parcels when they are sampled, or in the *source space*, that is at the location of the parcels when they are released. In the latter case, the parcels are further stratified according to the potential temperature of the parcels in the target space. In order to be independent of the arbitrary discretization, the convective impact is weighted for each convective parcel by  $\tau\delta^2\cos(\phi_S)$  where  $\tau$  is the time interval between two satellite images (1 hour),  $\delta$  is the size of the pixel in the satellite image ( $0.1^\circ$ ) and  $\phi_S$  is the latitude of the convective source. In the target space, the count is further multiplied by the sampling interval along the trajectory  $\Delta t = 6$  hours and is normalized by the mesh size in the target space that is  $\Delta\theta D^2\cos(\phi_T)$  where  $\phi_T$  is the mean latitude of the target cell. Hence the full normalization factor for the impact density in the target domain is  $\tau\Delta t\delta^2\cos(\phi_S)/\Delta\theta^2 D^2\cos(\phi_T)$ . The resulting quantity is called the impact density. In the source domain,  $\phi_T$  is replaced by  $\phi_S$  in the denominator and therefore the cosine factors disappear. The resulting quantity is called the source density. We define the cumulated impact as the integral of the convective impact density over the FullAMA domain for a given level.

As the impact density and the sourced density vary considerably with altitude, it is also useful to define an equalized quantity for the sake of comparison. This equalized quantity within a given domain is defined, for each pixel, as the ratio of the impact with respect to the value obtained by redistributing equally the cumulative impact over all pixels, according to their area.

Notice that each forward parcel is allowed to be counted as many times as it appears within the domain in the 6-hourly outputs during the integration period.

The impact can also be stratified according to the age, that is the time elapsed from the parcel release at the top of a convective cloud until its sampling. The cloud top distribution is equivalent to the impact at age 0.

The backward trajectories are analysed according to the probability of hitting a convective cloud within the integration time or exiting the FullAMA domain. The sources are counted on a mesh of one degree resolution in the horizontal and 1 K in the vertical. They are normalized and equalized in the same way as the forward sources. In the backward analysis, only the first hit is accounted.

The impact is not meant to be an estimate of the convective mass flux or the mixing ratio of convective air since we do not have any information on the detrainment at the top of observed clouds. It should be seen at a metric for convective influence which can be used to study how parcels originated from convection are confined, dispersed or diluted in the TTL.



### 3 Results

#### 3.1 Impact overview

We first present an overview of the impact in order to justify our approach. We use the ERA-Interim calculations to compare calculations made in the global domain and in the restricted FullAMA domain. Figure 2 shows the accumulated convective impact on the 380 K surface for parcels launched from the cloud tops over the period 1 June 2017 to 31 August 2017 with forward integration for two months. The air masses confinement inside the AMA is clearly visible and exhibits similar patterns in both the FullAMA and the global domain calculations for the ERA-Interim diabatic version (panels a & c). Over the FullAMA domain, the correlation between the impacts at 380 K in the two panels is 94.3% and on the average 96.9% between 340 K and 420 K (see Fig. 3). The ratio between the maximum impact for an integration restricted to the FullAMA domain, in panel (a), and the maximum impact in the FullAMA box for an integration in the global domain, in panel (c), is 0.91 at 380 K. It decays from 1 at 350 K to 0.8 at 420 K. Similarly, the ratio of the cumulated impacts over the FullAMA domain is 0.6 at 380 K and decays from 0.88 at 350 K to 0.52 at 420 K. At the same time, the total impact itself (shown in Fig. 4) decays by a factor 18 in the global calculation and 30 in the FullAMA calculations. The differences between the two calculations are due to parcels that leave the domain and disappear in the FullAMA calculations while re-entering the FullAMA domain in the global calculations. However, these parcels seldom re-enter the AMA core, hence the difference between the ratios of the maxima and of the cumulated impacts. As altitude rises, the cumulated impact decays strongly as a result of dynamical erosion of the AMA and this decay is much larger than the variation of the impact ratio between the global and the FullAMA calculations. Therefore we conclude that the confinement seen in the FullAMA calculations is not an effect of the boundaries and we will focus on this domain in most of the sequel. Further comparisons between the FullAMA and the global domain are made in the Supplement.

Figure 2 also shows the FullAMA impact for the ERA5 diabatic calculations (panel e). The pattern is again very similar to that of the ERA-Interim calculations in the panel (a) with a correlation of 99%, but the maximum impact and the cumulated impact are, respectively, reduced by a ratio 0.44 and 0.46. These results are due to the fact that the horizontal distribution of the impact depends essentially of the horizontal isentropic circulation which seldom differs between ERA-Interim and ERA5 while the amplitude ratio depends on the vertical motion which differs a lot.

Finally, Figure 2 shows the source density of convective parcels reaching the 380 K surface (panels b,d,f). The largest contribution in the FullAMA ERA-Interim calculations (panel b) comes from North India (mostly the Gange valley, Bengal and the north of the Bay of Bengal), with two other spots over the south of the Tibetan plateau and in South China. These areas are surrounded by a wide halo of sources mainly over the Asian continent but with some significant component over the Sea of China and the Pacific east of the Philippines. The distribution of the global sources (panel d) exhibits a general intensification, by about a factor 2, without changing the pattern of continental sources but also a shift towards a larger share of the maritime sources, that are much more intense relatively to the continental sources. The corresponding trajectories are travelling along the easterlies in the southern branch of the AMA and mostly leave the FullAMA domain without recirculating around or entering the AMA core.



The source distribution for the ERA5 is similar to that of the ERA-Interim but with important differences. The distribution is much more concentrated on the Gange valley and the Tibetan plateau with weakened contributions from Bengal and South China. The reinforcement of the Tibetan plateau is directly linked to the high penetrative convection above the plateau which is mentioned above in Sec. 2.1.

5 The source distribution shows a minimum over the narrow region which corresponds to the steep southern slope of the Himalayan plateau. The monsoon flow hitting this slope generates a lot of precipitations but does not lead to high convective towers that penetrate the TTL. This is not a feature of the 2017 season only but shows up also in a multi-year climatology of the high clouds (not shown). More generally, other areas providing a lot of monsoon precipitations like the Ghats in South India or the Arakan mountains are not visible in our source maps.

### 10 3.2 Vertical transport and erosion

Figure 4 upper panel shows the cumulated impact for the four FullAMA experiments (EAD, EAZ, EID, EIZ) compared to the high cloud distribution which is also the impact at age 0. The high cloud distribution in the FullAMA domain is the same for all experiments; it peaks strongly at  $\theta = 349.5$  K and is mostly distributed between 340 K and 370 K. Some rare convective events, however, are still found up to about 400 K in the stratosphere while the applied 250 hPa selection threshold produces a  
15 rapid cutoff in the lower layers below 335 K. The cumulated convective impact in the FullAMA domain peaks near the cloud peak. The maximum value of the impact distribution is located lower by a few degrees in potential temperature for the diabatic trajectories than for the kinematic trajectories and the cumulated impact below the cloud peak is also larger. The smallest peak for EID is associated with the smallest slope of the impact above the source peak and indicates that this case corresponds to the fastest upward transport. On the opposite, the largest peak for EIZ is associated with the largest slope. The two ERA5  
20 distributions exhibit intermediate results. We already see here, as it will be confirmed later, that EID and EIZ calculations exhibit large differences and bracket the two ERA-5 calculations which are much closer. Figure 4 right panel shows the distribution of the clouds together with the vertical profile of the heating rate, here reduced to the core AMA domain (20°E-140°E and 10°N-40°N), avoiding the boundaries of the FullAMA domain. It is visible that the zero level of radiative heating occurs above the maximum level of the sources, in a range of altitudes where the source density decays approximately exponentially with  
25 the potential temperature. The straight fit line shown in the figure corresponds to a decrement rate of  $0.325 \text{ K}^{-1}$ . As the ERA-Interim all sky heating crosses the zero axis at a lower altitude than ERA5 and provides stronger heating above 370 K, the ERA-Interim impact is expected to be stronger and to propagate faster upwards.

Figure 5 shows how the convective impact propagates inside the AMA domain from the sources as a function of age. In the kinematic and diabatic cases, the dispersion occurs both upward and downward. A clear separation occurs in the diabatic  
30 cases between the ascending and the descending branch, transporting parcels away from the main source level. The descending diabatic branch is very intense, ending at the imposed cutoff level. The upper branch exhibits a strong attenuation due to parcels exiting through the lateral boundaries, leading to the fast decay of the impact with altitude seen in Fig 4. The vertical propagation is the slowest for EIZ and the fastest for EID with the two ERA-5 cases in between and fairly close together. The propagation is estimated by fitting a straight line to the crests of the distribution on each isentropic layer. See also Sec. S4 in



the Supplement. The slope, denoted as  $A$  in the sequel, is found to be 1.08, 1.11, 0.97 and 1.35 K day<sup>-1</sup> for, respectively, EAZ, EAD, EIZ and EID. These values are consistent with the average heating rates of ERA5 and ERA-I (see Fig. 4) above 370 K. It is shown in Sec. S9 of the Supplement that this result is expected when diffusive transport by heating rate fluctuations can be neglected. The descending branch of the diabatic impact and the withdrawal of parcels from around the 350 K level is also  
5 consistent with the heating rate crossing from cooling to warming near this level in both reanalysis. The close proximity of the zero level of heating rate and of the maximum detrainment of the clouds is not fortuitous but can be seen as a manifestation of the Fixed Anvil Temperature principle (Hartmann and Larson, 2002).

As the vertical velocities are ascending everywhere in the monsoon region, the descending branch of the kinematic experiments which is quite clear in Fig. 5 must be located in another region. The descent occurs as a result of the horizontal westward  
10 transport of the AMA that brings the convective parcel over the Arabian desert and the Sahara where the air is subsiding (see Sec. S5 of the Supplement). This is one of the branches of the Hadley-Walker circulation during the monsoon season. The other branch that connects to the southern hemisphere is only implicit here but can be seen in the global experiments (see Sec. S7 of the Supplement).

The large differences between kinematic and diabatic trajectory transport properties in the ERA-Interim have already been  
15 noticed in a number of previous studies (e.g., Bergman et al., 2015; Bucci et al., 2019; Li et al., 2019).

Notice that the commonly used metric of the mean age might hinder the differences in vertical propagation. Figure 6 shows the normalized impact spectra taken from Fig. 5 at three vertical levels in the upper branch. The different separations of the modal peaks reproduce the differences in vertical propagation. However, the widening of the distributions is asymmetric and varies largely. The fastest propagation by EAD is associated by a narrow dispersion while the slowest propagation by EID is  
20 associated with a broad dispersion, the result being that the mean age separation, that is the mean age slope with altitude, is almost the same. The propagation and the dispersion in the ERA5 case are intermediate and the mean age slope remains close to the ERA-Interim value. This property is probably fortuitous and shows that the mean age metric is not reliable to estimate transport properties. We discuss below this observed behaviour and the possible reasons of the differences in Sec. 4 within the framework of a simple 1D model.

Figure 7 shows the decay of the total impact integrated over three isentropic layers as a function of age. At small ages, the  
25 impact is confined in the mid-layer, where the sources concentrate. Then the upper and lower layer impacts grow, the latter being rapidly dissipated by the bottom cut-off, so that eventually the upper layer impact dominates. The decay of the lower and mid layer impacts is much faster in the diabatic cases due to the descending motion within the source region. The asymptotic decay time scale  $\alpha$  of the upper layer is quite similar among EAD, EAZ and EID. It is larger for EIZ but the asymptotic  
30 limit, where the upper layer dominates, is only marginally reached in that case. We retain the value for ERA5 diabatic, that is  $\alpha = 13.3$  day as the erosion rate of the upper-layer. This time scale is of the order or smaller than the mean circulation rate in the AMA, two to three weeks, as found in Sec. S2 of the Supplement. Therefore the AMA exhibits only weak confinement properties. If we assume that this erosion rate and the mean vertical ascent  $A$  explain the dilution of the impact with altitude, we get a decay rate  $(\alpha A)^{-1} = 0.69$  K<sup>-1</sup> very close to the value 0.65 K<sup>-1</sup> obtained from Fig. 4.



In the sequel, we will focus on the ERA5 diabatic calculations. This set-up is shown to be the most relevant to interpret the airborne data of the StratoClim campaign by Bucci et al. (2019) and it produces results very close to the kinematic set-up as far as the upper branch of transport from the convective sources is concerned. More comparisons between diabatic and kinematic calculations and between FullAMA and global calculations can be found in the Supplement.

### 5 3.3 Horizontal distribution of impact and sources

In order to display how the confinement varies with altitude, Fig. 8 shows the impact distribution for four layer from 340 K to 370 K in the ERA5 diabatic calculations. In the lowest layers 340 K and 350 K (panels a and c), the convective parcels are rapidly expelled to other regions by the divergent motion which is maximum at these levels (see Fig. S4 of the Supplement) and to lower levels by diabatic cooling. Due to this combined effect, the impact is maximum at 340 K west of the monsoon region over the Arabian desert and the Sahara where the air is subsiding. This upper circulation from the monsoon uplift region is one of the main branches of the Hadley-Walker circulation during summer. Other descent regions in the southern hemisphere appear for global trajectory simulations corresponding to the other branches (see Fig. S9 of the Supplement). We stress that the descent branches are also observed for kinematic calculations, as seen in Figs. S7 and S9. However, as vertical velocities are positive over the whole tropospheric column in the monsoon region, the total descending impact is reduced with respect to the diabatic simulations. The distribution of sources for the 340 K and 350 K levels (see Fig. 8(b,d)) has a large maritime contribution, in particular over the Bay of Bengal (BoB), and the continental contribution concentrates over India in the eastern regions adjacent to the BoB.

A change occurs at 360 K with an impact pattern now centred over continental Asia (see Fig. 8(e)) and a distribution of the sources that concentrates over North India and the Tibetan plateau with maritime sources only on the North of the BoB (see Fig. 8(f)).

Figure 8(g,h) and Fig. 9 show that between 370 K and 420 K, the pattern remains basically constant both for the impact and for the sources, but for the exponential dilution shown in the upper panel of Fig.4, which is explained above as the combination of constant loss with uniform ascent over the AMA. The target pattern quite closely follows the contours of the Montgomery potential (see also Fig S2) that describes the main circulation within the domain.

Fig. 10 is produced from the backward EAD trajectories for the three months July-August-September 2017 within the FullAMA domain. The percentage of convective hits reaches 100% at 360K within a large region at the center of panel (a). This percentage decreases with altitude but remain high, with values above 80%, up to 380 K. At 400 K, a large majority of parcels leaves the FullAMA domain before reaching convection. Figure 10 also shows the source distribution in the horizontal and in the vertical. The parcels released at 360 K reach convection in a close neighbour of this level (panel c) and they show a mixed distribution of sources over the maritime and continental regions (panel b) like in Fig 8(f). For parcels released at higher levels the vertical distribution of sources broadens from near 360 K to the level of release (panels f, i, l). The distribution tends to peak near 365 K and is skewed with a sharp cutoff on the lower side and a longer tail on its upper side. The secondary peaks seen in the 380 K and 400 K distribution result from the discrete cloud top values produced by the SAF-NWC retrieval. The intensity of this peak at 400 K is an indication that rare events of penetrative convection might make a significant contribution



to the impact in the lower stratosphere. A better assessment of this penetrative convection is clearly needed to substantiate this finding. This is a challenge for present and future geostationary observations at high spatial and temporal resolution. The patterns of the horizontal distribution (panels e, h, k) are showing the same concentration of sources in North India and the Tibetan Plateau as for the forward case in Fig.4 with a decreasing contribution of over sources as the altitude rises.

### 5 3.4 Age

In forward runs, the age of air is calculated as the time interval between the parcel release from the cloud tops and the crossing of a given  $\theta$  level, multiple crossings being possible. In backward runs, the age of air is calculated as the time interval between the parcel release on the grid and the first hit of a convective cloud. The forward age is shown in Fig. 11 for both the target and the sources. At 350 K, panel (c) shows a meridional split between air younger than one week in the South and older air in the North. The young region spans the easterly jet that carries rapidly the maritime air produced over the Bay of Bengal and the Sea of China to the West over Africa and outside of the FullAMA domain. At 340 K (panel a), the age is 2 days or less where the impact concentrates south of the Bay of Bengal at very close proximity to the convective sources. The mean age is about 10 days over Sahara but much less over equatorial Africa. The age is larger in the core AMA region with a small impact due to the few parcels that recirculate within the AMA at this level. The pattern changes completely at 360 K (panel e) where a broad deep minimum age is seen at the core of the impact, surrounded by a region of larger age. The pattern persists at 380 K and 400 K (panels g and i) albeit with a much reduced contrast between the core and the periphery. Therefore, we conclude that the impact concentration within the AMA core is not related to trajectories being trapped and with long residence times but to the constant renewal by fresh convective air rising from below.

The distribution of age in the source space shows that at the lowest levels 340 K and 350 K (see Fig. 11(b,d)) the age is maximum over the continental regions and minimum over the maritime regions due to the fact that the continental air circulates within the AMA before being expelled towards the major subsident regions over Arabia and Africa, while the maritime air is directly transported to these regions. At 360 K and above (see panels f,h,j), the mean age is fairly uniformly distributed over the whole sources, indicating no preference for a faster path from any region. Similar results for the backward calculations are shown in Sec. S8 of the Supplement. Therefore we conclude that the age distribution indicates that the ascent occurs over a broad domain that covers the whole AMA rather than in a very localized region and that parcels remaining within the AMA spiral outward as they rise, as also found by Vogel et al. (2019).

### 3.5 Vertical crossover

In this section we concentrate on the domain where convection is the most active and relevant to the Asian monsoon. We divide this domain, labelled as Asia, into three subregions: Land, Ocean and Tibetan plateau as shown in Fig. 12. The Tibetan plateau is defined as the region with orography higher than 3800 m. We stress the need for a clear separation between ocean and land, that the commonly used rectangular boxes cannot provide. There are very noticeable differences, as shown in Tegtmeier et al. (2019b), in cloud properties and heating rates between the Bay of Bengal and the Sea of China on one side and the adjacent Indian subcontinent and South China on the other side.



Table 1 shows that the distribution of high clouds favours the Ocean (68.4%) rather than the Land (26.6%) and the Tibetan plateau (5%). The maritime convection is divided among the Sea of China and the Philippine Sea (23%), the West and Mid Pacific (17.1%), the Bay of Bengal (14%) and the Indian Ocean (10.8%). The land is divided among the Indian Subcontinent (12.8%), Indochina (7.8%) and South China (6.4%). The maximum high cloud covers lies on the the average 4 to 6 K higher on the Land than on the Ocean, and up to 10 K higher over the Tibetan Plateau.

Table 1 also shows the LZRH for ERA5 and ERA-Interim. In the ERA5 case, there is a separation of about 5 K between the LZRH and the mean high cloud level, while for ERA-Interim they are quite similar except over the Tibetan plateau where the LZRH remains higher by almost 8 K.

For the three regions and Asia as a whole, and for all source levels, we determine the proportion of trajectories, rising, descending or being stationary. In this purpose we divide the potential temperature range [322.5 K, 422.5 K] into 20 bins of width 5 K and we calculate for each region a 2D histogram for the source level and the mean level of the convective parcels during their life time. We then calculate the rising proportion, for each level, as the proportion of parcels borne in this level for which the mean potential temperature along their trajectory lies within bins located above this level. Similarly the descending proportion is calculated for parcels with mean level below the initial level and the stationary proportion corresponds to parcels with mean level within the initial bin.

Figure 13, drawn for the whole Asia region, shows a crossover at 362 K for both the FullAMA and global trajectories of EID. The crossover is located slightly above at 364 K for EAD, consistent with a smaller cloud radiative effect. At levels below the crossover, the two descent curves for EAD and EID within the FullAMA domain are very similar and drop rapidly due to the lower boundary. In the global domain, the drop is shifted to lower levels and delayed, due to a better representation of the cross-hemisphere Hadley-Walker circulation. The separation between ascending and descending motion near 360 K was already mentioned by Garny and Randel (2016).

Table 1 shows the crossovers for the three component regions. Over Land and Ocean, the crossover is above the LZRH by 4 K over Land and 4 K over Ocean. This is not true over the Tibetan plateau where it is below by 2 K for ERA5 and 3.5 K for ERA-Interim. The crossover remains, however, very close to that of the neighbour Land.

The fraction of the high clouds that are above the crossover and therefore contribute to the upward transport is quite low. It is minimum over Ocean (1.7% for ERA5). The Land value is more than double (5.1%) and the Tibetan plateau further doubles it (10.8%). As the ERA-Interim crossover is lower, the corresponding proportions are about twice that of ERA5. In both cases, continental convection is more likely than maritime convection to feed the upward motion above the LZRH and the Tibetan plateau is by far the most efficient region as already found by Tissier and Legras (2016).

As a result of the crossover pattern, and because maritime convection is more easily washed outside the FullAMA domain, the relative contribution of Ocean and Land to the FullAMA impact at 380 K is inverted with respect to the proportion of high clouds in these regions (see Table 1). For the ERA5, the ratio Ocean/Land for the high cloud proportion is 2.57, and 0.41 for the impact, therefore reduced by a ratio 0.16. This is partially explained by the crossover ratio of the high clouds, which is 0.33. The other explaining process is the washing out of the maritime impact. On the other side, the ratio Tibetan plateau/Land is 0.19 for the high cloud and 0.41 for the impact. The enhancement by a ratio 2.2 is entirely explained by the crossover ratio



which is 2.1. Similar numbers can be found for the ERA-Interim in the FullAMA domain. When we consider the global domain for the ERA-Interim, we see that the Ocean/Land impact ratio is 1.35, therefore a reduction by a ratio 0.52, slightly larger than the crossover ratio 0.4.

These results show that the enhanced impact of the Tibetan plateau is entirely due to the higher proportion of high clouds above the crossover in this region. The respective impact of oceanic versus land convection in the global domain is also mainly explained by this crossover proportion. There is more chance for parcels from continental convection to be trapped within the AMA but most of the air reaching the 380 K surface does not circulate first within the AMA. This result corroborates the findings of Tissier and Legras (2016) and Vogel et al. (2019).

#### 4 A simple model of AMA confinement

In this section we investigate how the observed behaviour of the impact in the FullAMA region can be represented by a simple 1D model. We consider a simple advection-diffusion model with loss for the impact  $F(\theta, t)$ :

$$\frac{\partial F}{\partial t} + \frac{\partial \dot{\theta} F}{\partial \theta} = -\alpha F + \kappa \frac{\partial^2 F}{\partial \theta^2} + S(\theta) \quad (1)$$

where  $\alpha$  is the erosion rate,  $\kappa$  is a vertical diffusion and  $S(\theta)$  account for the convective sources.

The profile of the heating rate in the lower panel of Fig. 4 suggests that we can separate a region near the LZRH  $\theta_0$  where the heating rate grows linearly with  $\theta$  and another region above where the heating rate is essentially constant. In addition, as the LZRH lies above the level of maximum high cloud, the source can be represented by an exponential distribution with the slope found in Fig. 4.

In the simplest version, we assume that  $\alpha = 0$ , therefore considering the global domain, and that the heating is  $\dot{\theta} = \Lambda(\theta - \theta_0)$ . In this case, (1) is a Fokker-Planck equation and it can be shown (Gardiner, 2009) that the probability of transit from  $\theta_a$  to  $\theta_b$  is

$$\Pi(\theta_a, \theta_b) = \frac{1 + \operatorname{erf}(\nu(\theta_a - \theta_0))}{1 + \operatorname{erf}(\nu(\theta_b - \theta_0))} \quad (2)$$

where  $\nu = (2\kappa)^{-1/2} \Lambda^{1/2}$ . Consequently, the distribution of convective sources that impact a given level is

$$P(\theta) = N^{-1} e^{-\beta(\theta - \theta_0)} (1 + \operatorname{erf}(\nu(\theta - \theta_0))) \quad (3)$$

where  $N$  is a constant. This distribution is plotted in Fig.14 and shows that, according to the value of the ratio  $\beta/\nu$ , the distribution of sources is centred on the LZRH, below it or above it. Table 1 shows that over Land and Ocean, the proportion of sources above the LZRH is always large, up to 96% over the Ocean. Therefore we are in the case where  $\beta > \nu$  and diffusion across the LZRH is negligible. The Tibetan plateau differs by exhibiting a majority of sources below the LZRH, especially for the ERA-Interim. This is consistent with the behaviour of the crossover and indicates that parcels rapidly travel outside the Tibetan plateau, where the LZRH is lower, and they find ascending motion. On the overall, this suggests that the LZRH is an



effective barrier and that diffusion due to fluctuating heating rates and explicit gravity waves resolved by the reanalysis do not allow to cross it.

In the second stage, we neglect diffusion and we assume that  $\dot{\theta} = \Lambda(\theta - \theta_0)$  from  $\theta_0$  to  $\theta_1$ , above which the heating rate is assumed to be constant equal to  $A = \Lambda(\theta_1 - \theta_0)$ . The LZRH is then a perfect barrier and we consider only the sources above  $\theta_0$ .

5 This problem can be fully solved (see Sect. S9 of the Supplement) and Figure S12 shows how the solution varies as a function of the parameter. A full interactive solution as a function of the parameters is available as a Computable Document Format notebook playable with Wolfram Player (<https://www.wolfram.com/player/>) as Supplementary material.

In the third stage, we calculate the solution by using the ERA5 and ERA-Interim heating within the AMACore region and the vertical distribution of sources used in the 3D calculations shown in Fig. 4. Figure 15 shows the distribution of impact as a function of age and potential temperature to be compared with the right column of Fig. 5. Here  $\kappa = 0.1 \text{ m}^2\text{s}^{-1}$  has been used to regularize the solution. The 1D model reproduces very well the main character of ascent and descent, albeit the temporal decay is faster than in the 3D calculations. A more quantitative comparison is made in Fig. 16 for ERA5 and the same three isentropic levels as Fig. 6, for several values of  $\kappa$ . We see that the diffusion basically slows the upward propagation but does not change qualitatively the solution. The 1D model shows results close enough to the 3D solution, providing a bulk explanation  
15 of the transport and confinement properties of the AMA.

## 5 Conclusions

We have studied the transport pathways from injection at the top of the high convective clouds to the lower tropical stratosphere during the Asian monsoon, using massive Lagrangian trajectories driven by observed clouds and reanalysis data. It has been shown that, unlike in the ERA-Interim, kinematic and diabatic trajectories of the ERA5 provide a consistent description of the motion above the LZRH. The kinematic and diabatic trajectories differ below the LZRH (missing in the kinematic case) within  
20 the convective region. However, both methods capture the descending motion over the deserts and the descending branches of the Hadley-Walker circulation.

There is a dichotomy among convective parcels which are injected above or below the crossover level. Below this level they are mostly entrained horizontally within the Hadley-Walker circulation towards regions of subsidence, where they return to lower levels. Above the crossover, parcels are entrained into the upward motion that lead them to cross the tropopause and enter the stratosphere. Only a small part of the convective clouds (2.6% on the average) reaches high enough, above the crossover, to inject parcels that move further upward. Due to the exponential decay of convective top frequency with altitude, the crossover is usually located above the LZRH, which appears as an effective barrier to vertical transport. The Tibetan plateau is an exception with a crossover lower than the LZRH but still close to that of surrounding land.

30 In the region above 360 K, the confinement within the AMA is the result of the constant renewal by fresh convective inflow and the leaky circulation of the AMA. As a result, the younger air is found at the core of the anticyclone and the oldest air is found at its periphery where it is expelled with a time-scale of about 13 days. This time is shorter than the returning time of



the mean circulation (about 2 to 3 weeks). As the level rises, the confined Asian monsoon air is more and more diluted and replaced by older air which comes from other regions.

The air that is trapped within the AMA comes mainly from continental convection. The sources exhibit a concentration in North India and the south of the Tibetan Plateau, as found in many previous studies (e.g., Bergman et al., 2015; Tissier and Legras, 2016). We find that, for continental convection as a whole, this result is partly due to the higher level of convection over land than over ocean.

The Tibetan plateau is favoured by its location at the core of the AMA and is also the region that exhibits the largest amount of high clouds above the crossover. This suggests that the compounds released at the ground there have the highest chance to reach the stratosphere. However, we find that the impact of the Tibetan plateau at 380 K is entirely explained by the high proportion of clouds above the crossover. There is no indication of a favoured ascent above the Tibetan clouds. On the contrary, the fact that the crossover is lower than the local LZRH indicates that parcels leave the Tibetan plateau to perform the ascent over other regions inside the AMA.

We find that the bulk properties of upward transport and confinement within the AMA over the whole summer can be explained by a simple 1D model, forced by the observed distribution of convective sources and heating rates and with a constant loss rate. The main ingredient to get an impact with both a maximum in age and altitude sections is that, between 360 K and 370 K, the heating grows from the LZRH and that it stays roughly constant above 370 K up to the lower stratosphere. This is entirely consistent with the other findings and the ascent within the AMA as a broad spiral, as advocated by Vogel et al. (2019), rather than concentrated in a narrow pipe.

Our diagnostics are based on whole summer averages and ignore the variability during the season. Section S10 of the Supplement touches that question and show that, at least in 2017, the pattern of the impact confinement does not change significantly over the whole summer, in spite of noticeable modulations in amplitudes and distribution within the AMA. The fact that the characteristic loss time is smaller than the circulation time indicates that the AMA confinement is fragile. It is modulated both by the source convective activity underneath, which is subject to a number of oscillations of the Monsoon, and by the modulation of filament shredding on the west and east edges which is also irregular, as discussed, e.g., in Pan et al. (2016) and Vogel et al. (2015).

The forward trajectories ignore possible intersections with clouds after launch. It has been shown by Tissier and Legras (2016) that accounting such effect has a very small effect on the statistics of upward motion which is here our main focus.

Our study is also limited by the quality of the observations and of the reanalysis. The estimation of high clouds from geostationary infra-red imagers is subject to a number of uncertainties, in particular due to the cover of semi-transparent cirrus clouds above the anvils. The SAF-NWC algorithm detects such features but there are discontinuities in cloud classification between MSG1 and Himawari-8 which have also a visible impact on the cloud height estimation. Combining imagers with sounders which are highly sensitive to ice clouds (Stubenrauch et al., 2013) will provide in the future a way to improve this retrievals.

The ERA5 was shown in several recent studies (Hoffmann et al., 2019; Tegtmeier et al., 2019a; Bucci et al., 2019) to provide a better representation of atmospheric properties, including transport. The ERA5 is, however, singular in favouring very high



penetrative convection over the Tibetan plateau which should be considered with caution due to the lack of data and of training of the model over this region.

The Tibetan plateau, in spite of its limited global impact, is a region of high interest to understand transport within the AMA. The lack of high quality observations with active instruments, both from the ground and from space (as current active  
5 instruments do not overpass the region in the evening when convection is the most active) hampers our understanding of convection over this region and certainly deserves some efforts to bridge the gap.

More generally, the fact that the clouds that contribute to the upward flux in the TTL and in the stratosphere are a small fraction within the upper tail distribution opens the question of the role of small-scale intermittent overshooting convection above the anvils which is seldom observed by the geostationary satellites. Although the effect was found by James et al. (2008)  
10 to be small in the Asian Monsoon region, this deserves further investigation within the context of Lagrangian studies.

On the overall, our estimates of the convective impact using high resolution datasets and advanced satellite products essentially corroborate that of Tissier and Legras (2016), made with lower resolution data and less advanced estimates of the high clouds. It is also in good qualitative agreement with Garny and Randel (2016) regarding the role of the crossover and with Orbe et al. (2015) and Vogel et al. (2019) regarding the distribution of sources.

15 *Code and data availability.* Most of the programs used in this study are freely available and documented under github bernard-legras. This study generated a multi-terabyte ensemble of trajectories and post-processed files stored on the Institut Pierre-Simon Laplace meso-centre. They are all available from the main author upon request.

*Author contributions.* The design of the experiments, Lagrangian calculations and data processing have been performed by B.L. The analysis and the writing of the manuscript have been performed by B.L and S.B.

20 *Competing interests.* The authors declare no conflict of interest

*Acknowledgements.* We thank Alexandra Tzella for pointing out the Gardiner's solution to the exit time problem. This work was supported by the StratoClim project by the European Community Seventh Framework Programme (FP7/2007–2013) under grant agreement no. 603557, and CEFIPRA 5607-1 and the TTL-Xing ANR-17-CE01-0015 projects. We thank the whole StratoClim Team for having made this successful campaign possible. Meteorological analysis data are provided by the European Centre for Medium-Range Weather Forecasts. ERA-5  
25 trajectory computations are generated using Copernicus Climate Change Service Information. We also thank the AERIS Data and Service Centre for providing access to the MSG1 and Himawari data and processing tools.



## References

- Bergman, J. W., Jensen, E. J., Pfister, L., and Yang, Q.: Seasonal Differences of Vertical-Transport Efficiency in the Tropical Tropopause Layer: On the Interplay between Tropical Deep Convection, Large-Scale Vertical Ascent, and Horizontal Circulations, *Journal of Geophysical Research*, 117, D05 302, <https://doi.org/10.1029/2011JD016992>, 2012.
- 5 Bergman, J. W., Fierli, F., Jensen, E. J., Honomichl, S., and Pan, L. L.: Boundary Layer Sources for the Asian Anticyclone: Regional Contributions to a Vertical Conduit, *Journal of Geophysical Research: Atmospheres*, 118, 2560–2575, <https://doi.org/10.1002/jgrd.50142>, 2013.
- Bergman, J. W., Pfister, L., and Yang, Q.: Identifying Robust Transport Features of the Upper Tropical Troposphere, *Journal of Geophysical Research: Atmospheres*, 120, 6758–6776, <https://doi.org/10.1002/2015JD023523>, 2015.
- 10 Berry, E. and Mace, G. G.: Cloud Properties and Radiative Effects of the Asian Summer Monsoon Derived from A-Train Data, *Journal of Geophysical Research: Atmospheres*, 119, 9492–9508, <https://doi.org/10.1002/2014JD021458>, 2014.
- Bucci, S., Legras, B., Sellitto, P., D’Amato, F., Viciani, S., Montori, A., Chiarugi, A., Ravegnani, F., Ulanovsky, A., Cairo, F., and Stroh, F.: Deep Convective Influence on the UTLS Composition in the Asian Monsoon Anticyclone Region: 2017 StratoClim Campaign Results, *Atmospheric Chemistry and Physics Discussion*, submitted, 2019.
- 15 Copernicus Climate Change Service (C3S): ERA5: Fifth Generation of ECMWF Atmospheric Reanalyses of the Global Climate, Tech. rep., Copernicus Climate Change Service Climate Data Store (CDS), 2017.
- Corti, T., Luo, B. P., Fu, Q., Vömel, H., and Peter, T.: The Impact of Cirrus Clouds on Tropical Troposphere-to-Stratosphere Transport, *Atmospheric Chemistry and Physics*, 6, 2539–2547, <https://doi.org/10.5194/acp-6-2539-2006>, 2006.
- Dee, D. P., Uppala, S. M., Simmons, A. J., Berrisford, P., Poli, P., Kobayashi, S., Andrae, U., Balmaseda, M. A., Balsamo, G., Bauer, P., Bechtold, P., Beljaars, A. C. M., Van de Berg, L. V. D., Bidlot, J., Bormann, N., Delsol, C., Dragani, R., Fuentes, M., Geer, A. J., Haimberger, L., Healy, S. B., Hersbach, H., Hólm, E. V., Isaksen, I., Kållberg, P., Köhler, M., Matricardi, M., McNally, A. P., Monge-Sanz, B. M., Morcrette, J. J., Park, B.-K., Peubey, C., de Rosnay, P., Tavolato, C., Thépaut, J.-N., and Vitart, F.: The ERA-Interim Reanalysis : Configuration and Performance of the Data Assimilation System, *Quarterly Journal of the Royal Meteorological Society*, 137, 553–597, <https://doi.org/10.1002/qj.828>, 2011.
- 20 Derrien, M. and Le Gléau, H.: Improvement of Cloud Detection near Sunrise and Sunset by Temporal-Differencing and Region-Growing Techniques with Real-Time SEVIRI, *International Journal of Remote Sensing*, 31, 1765–1780, <https://doi.org/10.1080/01431160902926632>, 2010.
- Fan, Q., Bian, J., and Pan, L. L.: Stratospheric Entry Point for Upper-Tropospheric Air within the Asian Summer Monsoon Anticyclone, *Science China Earth Sciences*, 60, 1685–1693, <https://doi.org/10.1007/s11430-016-9073-5>, 2017.
- 30 Fueglistaler, S., Dessler, A. E., Dunkerton, T. J., Folkins, I., Fu, Q., and Mote, P. W.: Tropical Tropopause Layer, *Reviews of Geophysics*, 47, RG1004, <https://doi.org/10.1029/2008RG000267>, 2009.
- Gardiner, C. W.: *Stochastic Methods: A Handbook for the Natural and Social Sciences*, Springer Series in Synergetics, Springer, Berlin, 4th edn., 2009.
- Garny, H. and Randel, W. J.: Dynamic Variability of the Asian Monsoon Anticyclone Observed in Potential Vorticity and Correlations with Tracer Distributions, *Journal of Geophysical Research: Atmospheres*, 118, 13,421–13,433, <https://doi.org/10.1002/2013JD020908>, 2013.
- Garny, H. and Randel, W. J.: Transport Pathways from the Asian Monsoon Anticyclone to the Stratosphere, *Atmospheric Chemistry and Physics*, 16, 2703–2718, <https://doi.org/10.5194/acp-16-2703-2016>, 2016.



- Hartmann, D. L. and Larson, K.: An Important Constraint on Tropical Cloud - Climate Feedback, *Geophysical Research Letters*, 29, 1951–1951, <https://doi.org/10.1029/2002GL015835>, 2002.
- Hoffmann, L., Günther, G., Li, D., Stein, O., Wu, X., Griessbach, S., Heng, Y., Konopka, P., Müller, R., Vogel, B., and Wright, J. S.: From ERA-Interim to ERA5: The Considerable Impact of ECMWF's next-Generation Reanalysis on Lagrangian Transport Simulations, *Atmospheric Chemistry and Physics*, 19, 3097–3124, <https://doi.org/10.5194/acp-19-3097-2019>, 2019.
- James, R., Bonazzola, M., Legras, B., Surbled, K., and Fueglistaler, S.: Water Vapor Transport and Dehydration above Convective Outflow during Asian Monsoon, *Geophysical Research Letters*, 35, L20 810, <https://doi.org/10.1029/2008GL035441>, 2008.
- Johansson, E., Devasthale, A., L'Ecuyer, T., Ekman, A. M. L., and Tjernström, M.: The Vertical Structure of Cloud Radiative Heating over the Indian Subcontinent during Summer Monsoon, *Atmospheric Chemistry and Physics*, 15, 11 557–11 570, <https://doi.org/10.5194/acp-15-11557-2015>, 2015.
- Li, D., Vogel, B., Müller, R., Bian, J., Günther, G., Plöger, F., Li, Q., Zhang, J., Bai, Z., Vömel, H., and Riese, M.: Dehydration and Low Ozone in the Tropopause Layer over the Asian Monsoon Caused by Tropical Cyclones: Lagrangian Transport Calculations Using ERA-Interim and ERA5 Reanalysis Data, Preprint, *Dynamics/Atmospheric Modelling/Troposphere/Physics (physical properties and processes)*, <https://doi.org/10.5194/acp-2019-816>, 2019.
- Luo, J., Pan, L. L., Honomichl, S. B., Bergman, J. W., Randel, W. J., Francis, G., Clerbaux, C., George, M., Liu, X., and Tian, W.: Space–Time Variability in UTLS Chemical Distribution in the Asian Summer Monsoon Viewed by Limb and Nadir Satellite Sensors, *Atmospheric Chemistry and Physics*, 18, 12 511–12 530, <https://doi.org/10.5194/acp-18-12511-2018>, 2018.
- McFarlane, S. A., Mather, J. H., and Ackerman, T. P.: Analysis of Tropical Radiative Heating Profiles: A Comparison of Models and Observations, *Journal of Geophysical Research*, 112, D14 218, <https://doi.org/10.1029/2006JD008290>, 2007.
- Orbe, C., Waugh, D. W., and Newman, P. A.: Air-Mass Origin in the Tropical Lower Stratosphere: The Influence of Asian Boundary Layer Air, *Geophysical Research Letters*, 42, 4240–4248, <https://doi.org/10.1002/2015GL063937>, 2015.
- Pan, L. L., Honomichl, S. B., Kinnison, D. E., Abalos, M., Randel, W. J., Bergman, J. W., and Bian, J.: Transport of Chemical Tracers from the Boundary Layer to Stratosphere Associated with the Dynamics of the Asian Summer Monsoon, *Journal of Geophysical Research: Atmospheres*, 121, 14,159–14,174, <https://doi.org/10.1002/2016JD025616>, 2016.
- Park, M., Randel, W. J., Gettelman, A., Massie, S. T., and Jiang, J. H.: Transport above the Asian Summer Monsoon Anticyclone Inferred from Aura Microwave Limb Sounder Tracers, *Journal of Geophysical Research*, 112, D16 309–D16 309, <https://doi.org/10.1029/2006JD008294>, 2007.
- Park, M., Randel, W. J., Emmons, L. K., Bernath, P. F., Walker, K. A., and Boone, C. D.: Chemical Isolation in the Asian Monsoon Anticyclone Observed in Atmospheric Chemistry Experiment (ACE-FTS) Data, *Atmospheric Chemistry and Physics*, 8, 757–764, <https://doi.org/10.5194/acp-8-757-2008>, 2008.
- Park, M., Randel, W. J., Emmons, L. K., and Livesey, N. J.: Transport Pathways of Carbon Monoxide in the Asian Summer Monsoon Diagnosed from Model of Ozone and Related Tracers (MOZART), *Journal of Geophysical Research*, 114, D08 303–D08 303, <https://doi.org/10.1029/2008JD010621>, 2009.
- Pisso, I. and Legras, B.: Turbulent Vertical Diffusivity in the Sub-Tropical Stratosphere, *Atmospheric Chemistry and Physics*, 8, 697–707, <https://doi.org/10.5194/acp-8-697-2008>, 2008.
- Ploeger, F., Gottschling, C., Griessbach, S., Groß, J.-U., Guenther, G., Konopka, P., Müller, R., Riese, M., Strohm, F., Tao, M., Ungermann, J., Vogel, B., and von Hobe, M.: A Potential Vorticity-Based Determination of the Transport Barrier in the Asian Summer Monsoon Anticyclone, *Atmospheric Chemistry and Physics*, 15, 13 145–13 159, <https://doi.org/10.5194/acp-15-13145-2015>, 2015.



- Ploeger, F., Konopka, P., Walker, K., and Riese, M.: Quantifying Pollution Transport from the Asian Monsoon Anticyclone into the Lower Stratosphere, *Atmospheric Chemistry and Physics*, 17, 7055–7066, <https://doi.org/10.5194/acp-17-7055-2017>, 2017.
- Randel, W. J. and Jensen, E. J.: Physical Processes in the Tropical Tropopause Layer and Their Roles in a Changing Climate, *Nature Geoscience*, 6, 169–176, <https://doi.org/10.1038/ngeo1733>, 2013.
- 5 Randel, W. J. and Park, M.: Deep Convective Influence on the Asian Summer Monsoon Anticyclone and Associated Tracer Variability Observed with Atmospheric Infrared Sounder (AIRS), *Journal of Geophysical Research*, 111, D12314–D12314, <https://doi.org/10.1029/2005JD006490>, 2006.
- Randel, W. J., Park, M., Wu, F., and Livesey, N.: A Large Annual Cycle in Ozone above the Tropical Tropopause Linked to the Brewer–Dobson Circulation, *Journal of the Atmospheric Sciences*, 64, 4479–4488, <https://doi.org/10.1175/2007JAS2409.1>, 2007.
- 10 Randel, W. J., Park, M., Emmons, L., Kinnison, D., Bernath, P., Walker, K., Boone, C., and Pumphrey, H.: Asian Monsoon Transport of Pollution to the Stratosphere., *Science*, 328, 611–613, <https://doi.org/10.1126/science.1182274>, 2010.
- Santee, M. L., Manney, G. L., Livesey, N. J., Schwartz, M. J., Neu, J. L., and Read, W. G.: A Comprehensive Overview of the Climatological Composition of the Asian Summer Monsoon Anticyclone Based on 10 Years of Aura Microwave Limb Sounder Measurements, *Journal of Geophysical Research: Atmospheres*, 122, 5491–5514, <https://doi.org/10.1002/2016JD026408>, 2017.
- 15 Sèze, G., Pelon, J., Derrien, M., Le Gléau, H., and Six, B.: Evaluation against CALIPSO Lidar Observations of the Multi-Geostationary Cloud Cover and Type Dataset Assembled in the Framework of the Megha-Tropiques Mission: Evaluation of a Multi-Geostationary Cloud Cover Set Using CALIOP Data, *Quarterly Journal of the Royal Meteorological Society*, 141, 774–797, <https://doi.org/10.1002/qj.2392>, 2015.
- Stohl, A., Forster, C., Frank, A., Seibert, P., and Wotawa, G.: Technical Note: The Lagrangian Particle Dispersion Model FLEXPART Version 6.2, *Atmospheric Chemistry and Physics*, 5, 2461–2474, <https://doi.org/10.5194/acp-5-2461-2005>, 2005.
- 20 Stubenrauch, C. J., Rossow, W. B., Kinne, S., Ackerman, S., Cesana, G., Chepfer, H., Di Girolamo, L., Getzewich, B., Guignard, A., Heidinger, A., Maddux, B. C., Menzel, W. P., Minnis, P., Pearl, C., Platnick, S., Poulsen, C., Riedi, J., Sun-Mack, S., Walther, A., Winker, D., Zeng, S., and Zhao, G.: Assessment of Global Cloud Datasets from Satellites: Project and Database Initiated by the GEWEX Radiation Panel, *Bulletin of the American Meteorological Society*, 94, 1031–1049, <https://doi.org/10.1175/BAMS-D-12-00117.1>, 2013.
- Tegtmeier, S., Anstey, J., Davis, S., Dragani, R., Harada, Y., Ivanciu, I., Pilch Kedzierski, R., Krüger, K., Legras, B., Long, C., Wang, J. S., Wargan, K., and Wright, J. S.: The Tropical Tropopause Layer in Reanalysis Data Sets, *Atmospheric Chemistry and Physics Discussions*, pp. 1–28, <https://doi.org/10.5194/acp-2019-580>, 2019a.
- Tegtmeier, S., Krüger, K., Birner, T., Davis, N. A., Davis, S., Fujiwara, M., Homeyer, C. R., Ivanciu, I., Kim, Y.-H., Legras, B., Manney, G. L., Nishimoto, E., Nützel, M., Kedzierski, R. P., Wang, J. S., Wang, T., and Wright, J. S.: Tropical Tropopause Layer, Stratosphere-Troposphere Processes And Their Role in Climate, Chapter 8, Submitted, (SPARC) Reanalysis Intercomparison Project (S-RIP) Report,
- 30 2019b.
- Tissier, A.-S. and Legras, B.: Convective Sources of Trajectories Traversing the Tropical Tropopause Layer, *Atmospheric Chemistry and Physics*, 16, 3383–3398, <https://doi.org/10.5194/acp-16-3383-2016>, 2016.
- Tzella, A. and Legras, B.: A Lagrangian View of Convective Sources for Transport of Air across the Tropical Tropopause Layer: Distribution, Times and the Radiative Influence of Clouds, *Atmospheric Chemistry and Physics*, 11, 12517–12534, <https://doi.org/10.5194/acp-11-12517-2011>, 2011.
- 35 Vernier, J.-P., Fairlie, T. D., Natarajan, M., Wienhold, F. G., Bian, J., Martinsson, B. G., Crumeyrolle, S., Thomason, L. W., and Bedka, K. M.: Increase in Upper Tropospheric and Lower Stratospheric Aerosol Levels and Its Potential Connection with Asian Pollution: ATAL Nature and Origin, *Journal of Geophysical Research: Atmospheres*, 120, 1608–1619, <https://doi.org/10.1002/2014JD022372>, 2015.



- Vogel, B., Günther, G., Müller, R., Groß, J.-U., and Riese, M.: Impact of Different Asian Source Regions on the Composition of the Asian Monsoon Anticyclone and of the Extratropical Lowermost Stratosphere, *Atmospheric Chemistry and Physics*, 15, 13 699–13 716, <https://doi.org/10.5194/acp-15-13699-2015>, 2015.
- Vogel, B., Müller, R., Günther, G., Spang, R., Hanumanthu, S., Li, D., Riese, M., and Stiller, G. P.: Lagrangian Simulations of the Transport of Young Air Masses to the Top of the Asian Monsoon Anticyclone and into the Tropical Pipe, *Atmospheric Chemistry and Physics*, 19, 6007–6034, <https://doi.org/10.5194/acp-19-6007-2019>, 2019.
- Wright, J. S. and Fueglistaler, S.: Large Differences in Reanalyses of Diabatic Heating in the Tropical Upper Troposphere and Lower Stratosphere, *Atmospheric Chemistry and Physics*, 13, 9565–9576, <https://doi.org/10.5194/acp-13-9565-2013>, 2013.
- Wright, J. S., Fu, R., Fueglistaler, S., Liu, Y. S., and Zhang, Y.: The Influence of Summertime Convection over Southeast Asia on Water Vapor in the Tropical Stratosphere, *Journal of Geophysical Research*, 116, D12 302, <https://doi.org/10.1029/2010JD015416>, 2011.
- Yan, R. and Bian, J.: Tracing the Boundary Layer Sources of Carbon Monoxide in the Asian Summer Monsoon Anticyclone Using WRF-Chem, *Advances in Atmospheric Sciences*, 32, 943–951, <https://doi.org/10.1007/s00376-014-4130-3>, 2015.
- Yang, Q., Fu, Q., and Hu, Y.: Radiative Impacts of Clouds in the Tropical Tropopause Layer, *Journal of Geophysical Research*, 115, D00H12, <https://doi.org/10.1029/2009JD012393>, 2010.

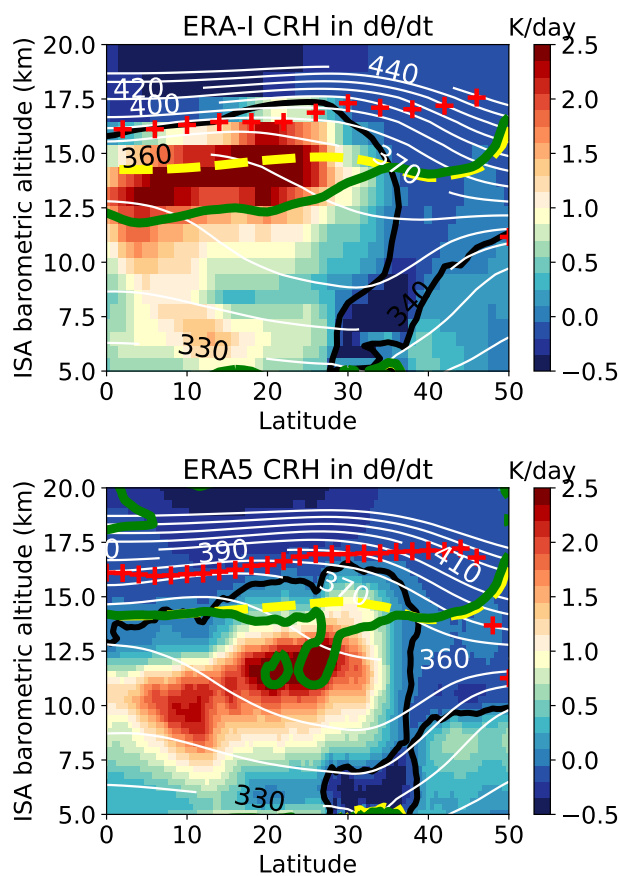


**Figure 1.** Cloud radiative heating (CRH) contribution to  $d\theta/dt$  (in  $\text{K day}^{-1}$ ) averaged over July-August 2017 in the  $73^{\circ}\text{E}$ - $97^{\circ}\text{E}$  longitude range. Upper panel: ERA-Interim. Lower panel: ERA5. The black contour shows the zero line of CRH. White contours show potential temperature (in K). Red crosses show the cold point tropopause. The yellow line shows the level of zero clear sky radiative heating. The green contour shows the level of zero all sky radiative heating (LZRH). The vertical axis is the barometric altitude derived from pressure using the hydrostatic equation and the standard atmosphere. The true geopotential altitude is higher, up to +850 m on the 360 K surface near 30N (see Fig. S1 of the Supplement).

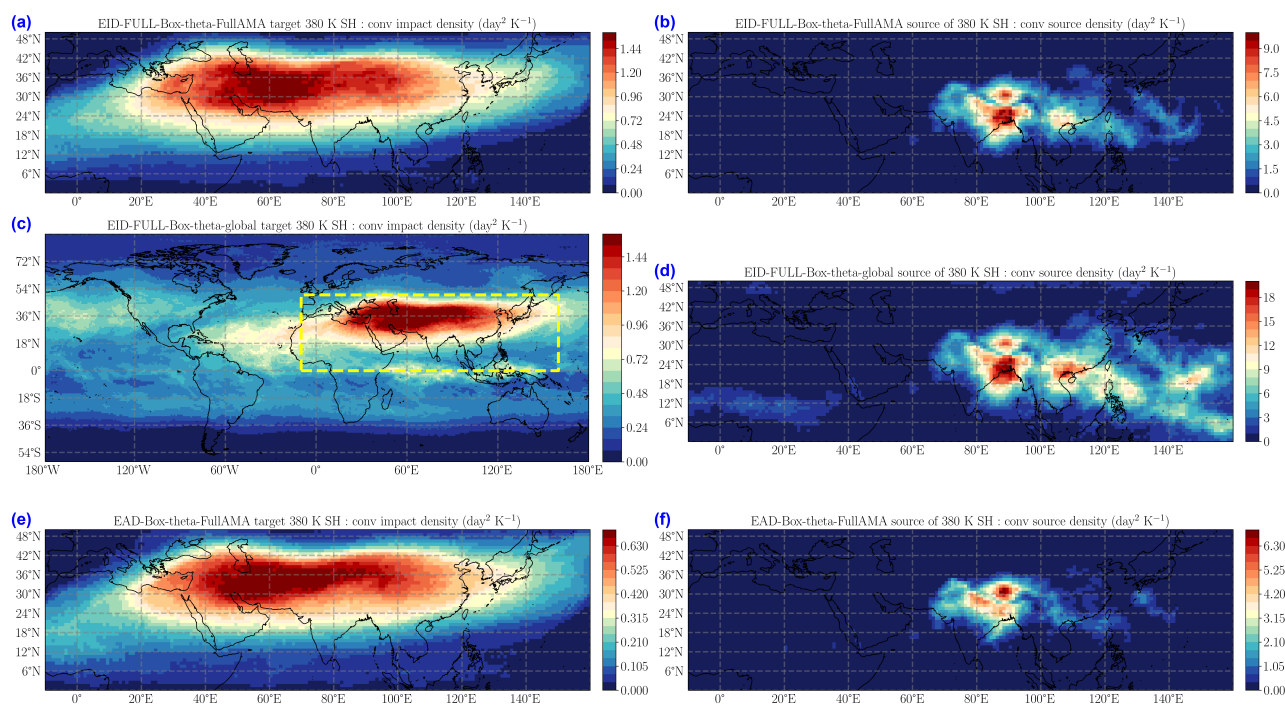


**Figure 2.** Impact density and source density for the convective parcels reaching the 380 K target level, accumulated over the 1 June 2017 to 31 August 2017 launch interval and the two-month life time of the parcels. Left column (a,c,d): the impact density at the 380 K target level. Right column (b,c,e): the source density of convective clouds from which the parcels reaching 380 K have been launched. Upper row (a,b): ERA-Interim diabatic trajectories in the FullAMA domain. Mid-row (c,d): ERA-Interim diabatic trajectories in the global domain. Lower row (e,f): ERA5 diabatic trajectories in the FullAMA domain.

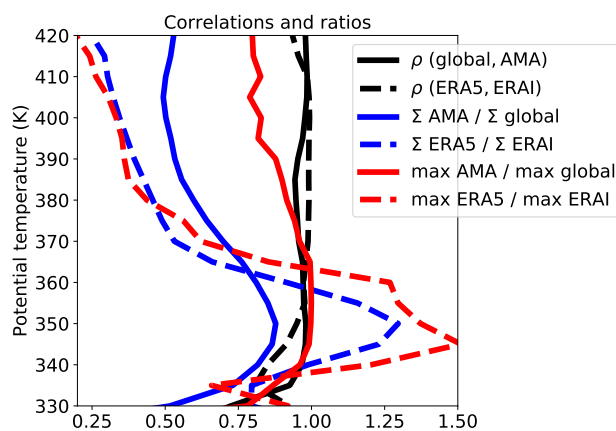


**Figure 3.** Solid back: correlation of the impact density between FullAMA and global EID calculations within the FullAMA domain. Dash black: same for EAD and EID FullAMA calculations. Solid blue: ratio of maximum impacts between the FullAMA and global EID calculations within the FullAMA domain. Dash blue: same for EAD and EID FullAMA calculations. Solid red: ratio of cumulated impacts between the FullAMA and global EID calculations within the FullAMA domain. Dash blue: same for EAD and EID FullAMA calculations.

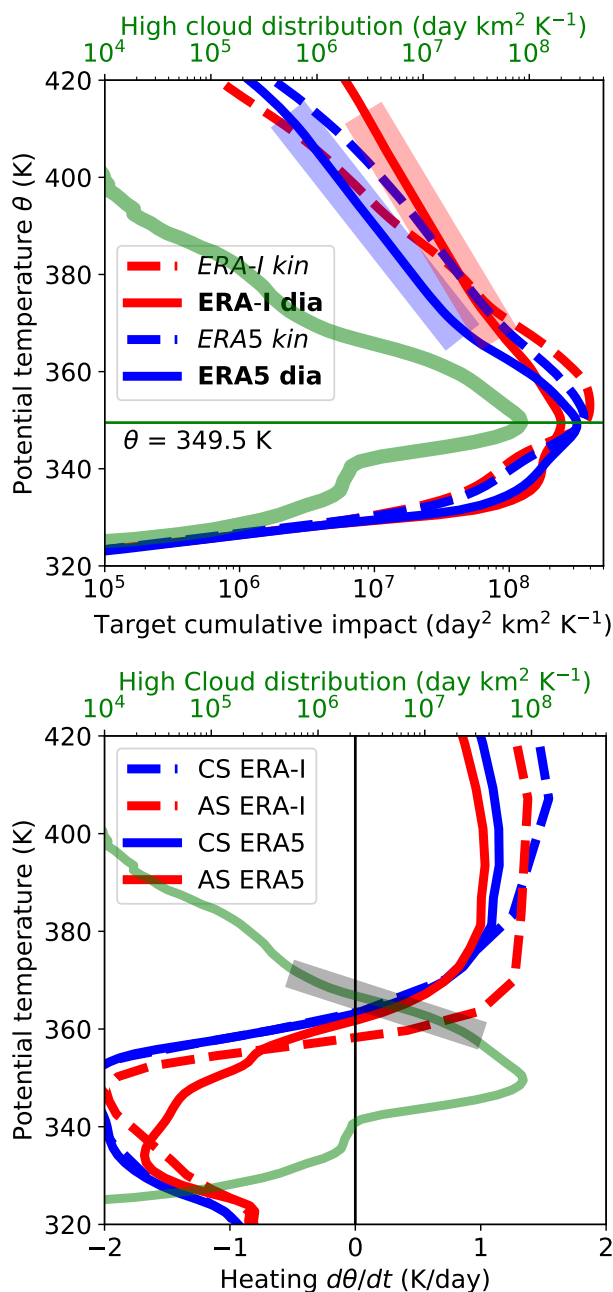


**Figure 4.** Upper panel. Green: Vertical distribution of the selected high cloud tops. Other curves: vertical distribution of the impact integrated within the FullAMA domain for the EAD (solid blue), EAZ (dash blue), EID (solid red) and EIZ (dash red) experiments. For EAD and EID, a fit with a logarithmic decrement, respectively  $0.065 \text{ K}^{-1}$  and  $0.050 \text{ K}^{-1}$ , is shown between 370 K and 400 K.

Lower panel. Green: same as in upper panel. Other curves: radiative heating rate profile average over the CoreAMA domain ( $10^\circ\text{E} - 140^\circ\text{E}$ ,  $10^\circ\text{N} - 40^\circ\text{N}$ ) where the sources concentrate for July and August 2017 for all sky ERA5 (solid red), all sky ERA-Interim (dash red), clear sky ERA5 (solid blue) and clear sky ERA-Interim (dash blue). The fit of the high cloud distribution between 360 K and 370 K is shown with a logarithmic decrement  $\beta = 0.325 \text{ K}^{-1}$ .

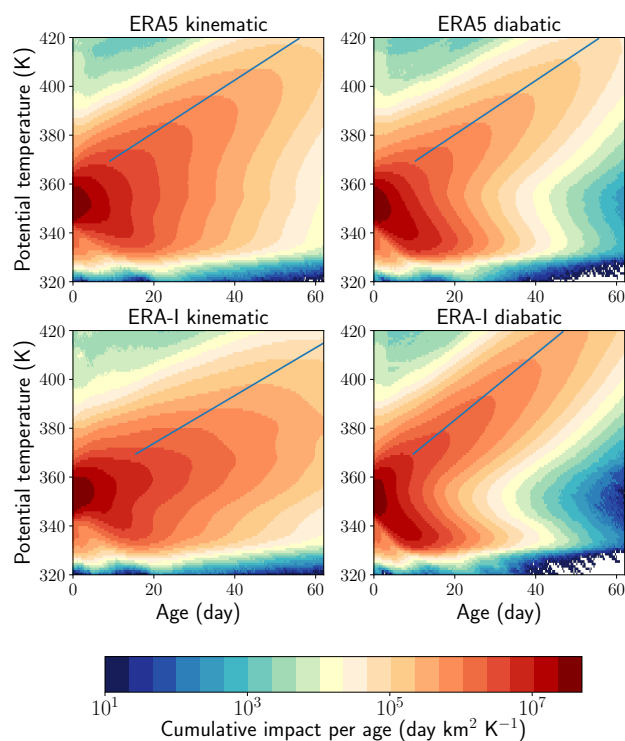


**Figure 5.** Distribution of the cumulated impact as a function of altitude and age with respect to the launch of the convective parcels. Upper row: ERA5. Lower row ERA-Interim. Left column: kinematic trajectories. Right column: diabatic trajectories. The slopes are taken from Sect. S4 of the Supplement.

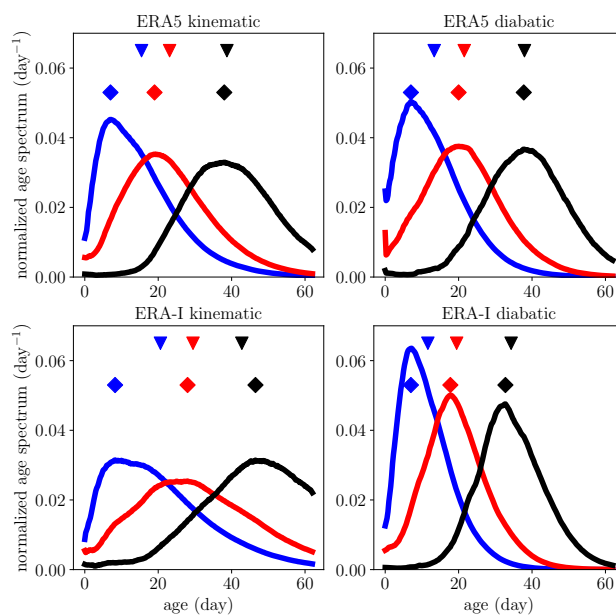


**Figure 6.** Normalized distribution of the ages among convective parcels within the FullAMA domain at three isentropic levels 370 K (blue), 380 K (red) and 400 K (black). The diamonds and the triangles show, respectively, the modal and the mean age for each curve. The four panels are arranged as in Fig. 5.

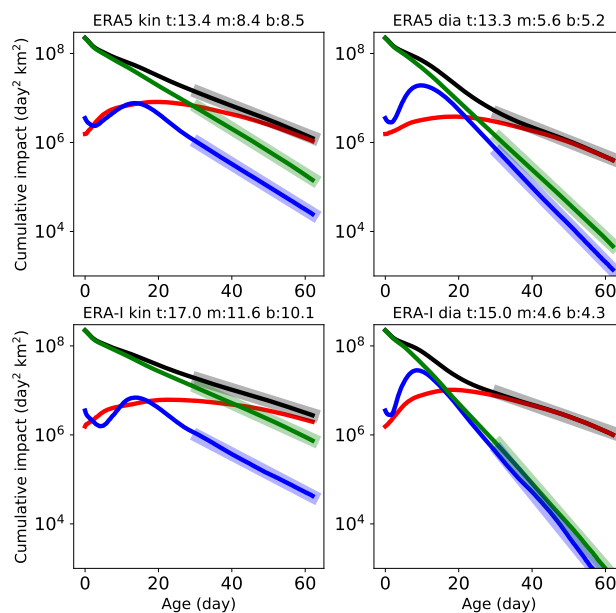


**Figure 7.** Evolution, as a function of age, of the total impact (black), the lower layer impact for  $\theta < 340$  K, the mid-layer impact for  $340 \text{ K} < \theta < 370 \text{ K}$  and the upper layer impact for  $370 \text{ K} < \theta$ . The four panels are arranged as in Fig. 5. The asymptotic e-folding time of the total and upper layer for the four cases are 13.4, 13.3, 17.0 and 15 day for, respectively, EAZ, EAD, EIZ and EID. The asymptotic e-folding times (in days) for the top-layer (t), mid-layer (m) and bottom-layer (b) are listed in the title of each panel.

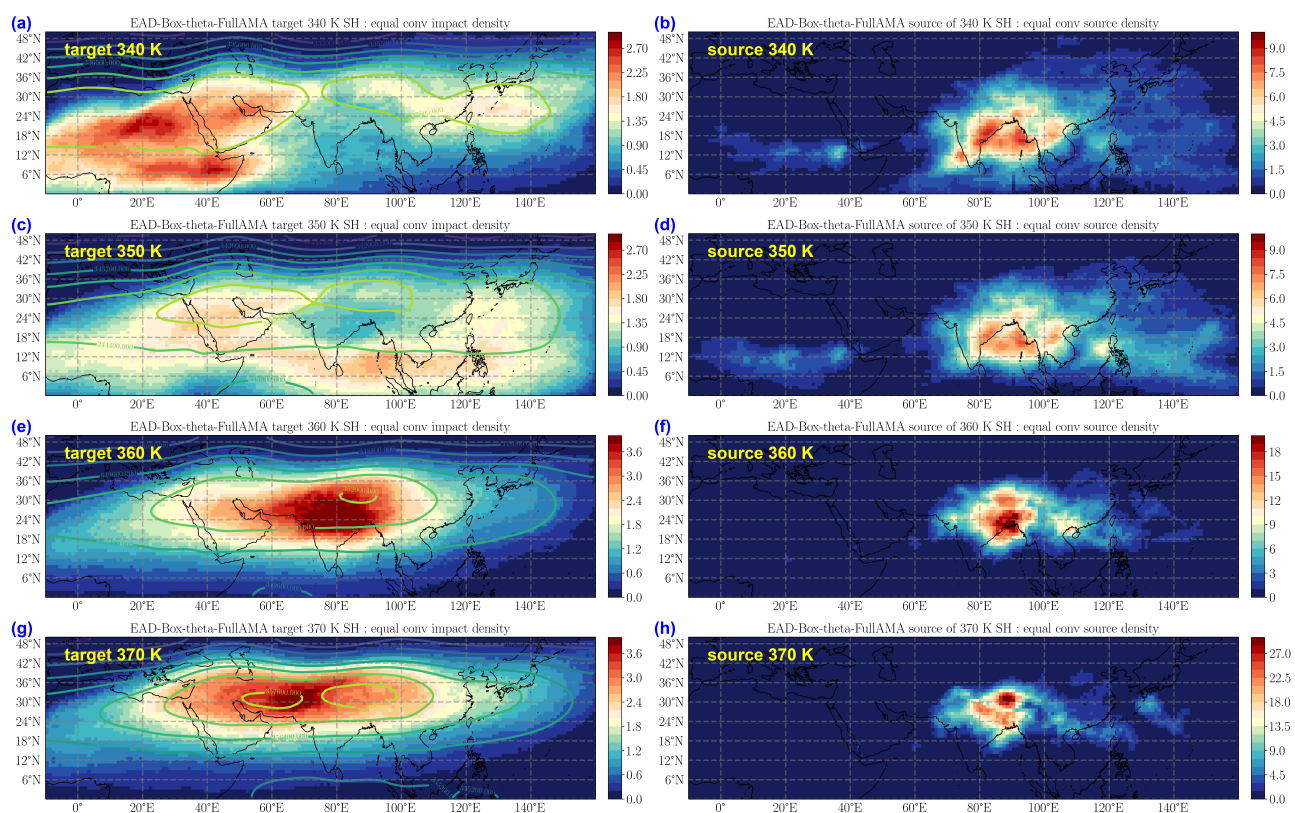


**Figure 8.** Left column (a,c,e,g): equalized impact density on isentropic levels (from top to bottom) (a) 340 K, (c) 350 K, (e) 360 K and (g) 370 K for ERA5 diabatic trajectories. Contours: Montgomery potential at the same levels. Right column (b,d,f,h): equalized source density for the same levels as in the left column and the same experiment.

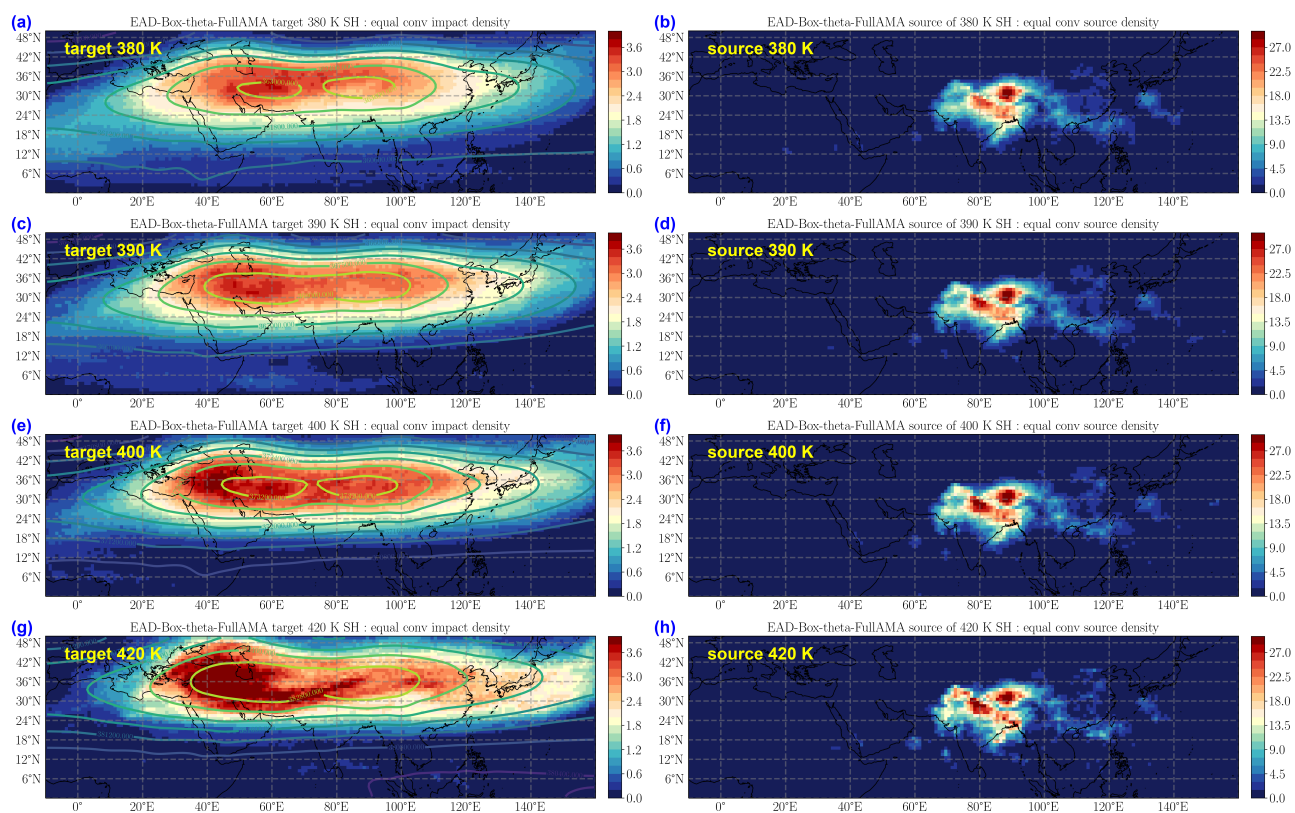


**Figure 9.** Same as Fig. 8 but for the levels (from top to bottom) 380 K, 390 K, 400 K and 420 K.

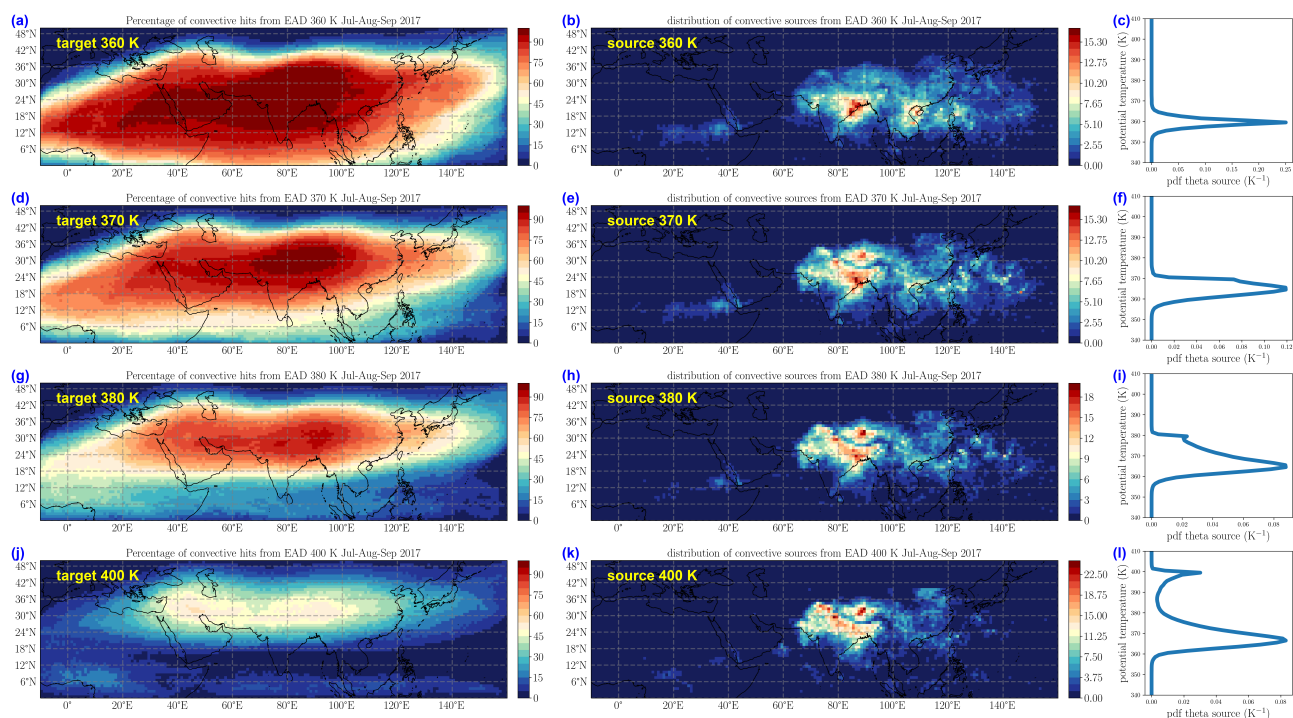


**Figure 10.** Left column (a,d,g,j): percentage of parcels hitting a convective cloud within 44 days of ERA5 diabatic backward trajectory starting at 380 K (a), 390 K (b), 400 K (g) and 420 K (j) over the interval 1 July - 30 September 2017. Center column (b,e,h,k): equalized source density for the same levels as in the left column and the same experiment. Right column: vertical probability density function (in  $\text{K}^{-1}$ ) of the cumulated source density for the same levels as the two left other columns.

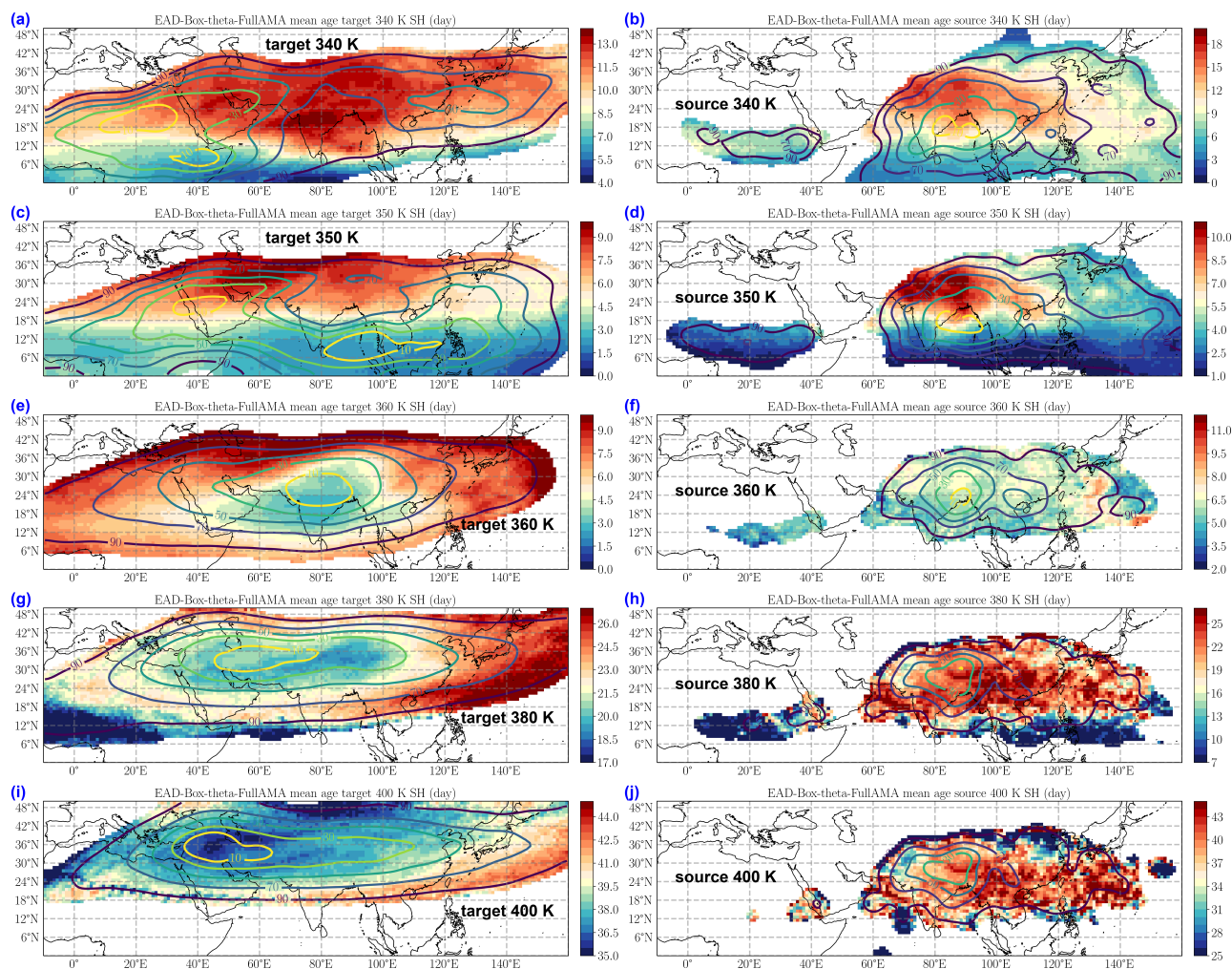


**Figure 11.** Left column (a,c,e,g,i): mean age (in Day) with respect to convection for forward parcels reaching the levels 340 K (a), 350 K (c), 360 K (e), 380 K (g) and 400 K (i). Right column (b,d,f,h,j): mean age in the source domain for the same parcels as in the left column for each level.

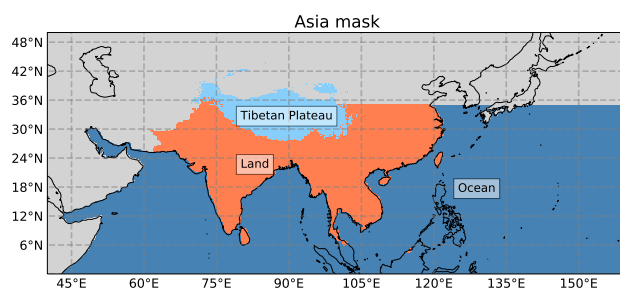


**Figure 12.** Mask of the three regions that partition Asia defined as their union.

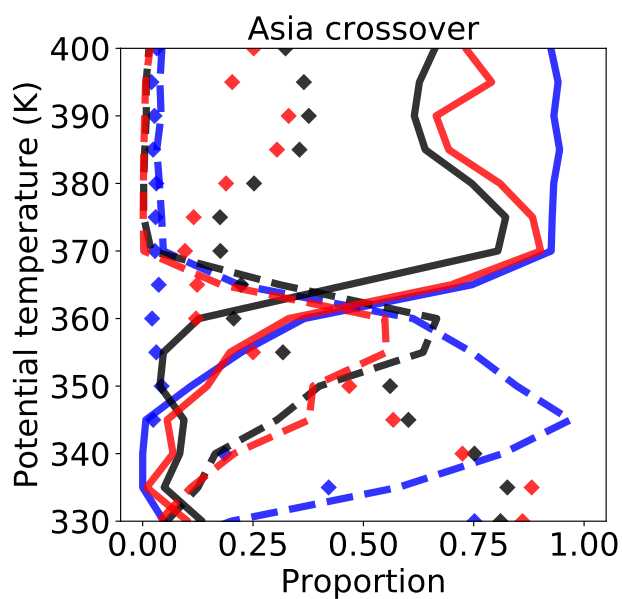


**Figure 13.** Solid and dashed curves: proportion of forward trajectories for which the mean vertical position during life-time is in a 5 K bin, respectively above or below, that of origin. Diamonds: proportion of forward trajectories with a mean vertical position within the origin 5 K bin. Black: ERA5 in the FullAMA domain; Red: ERA-Interim in the FullAMA domain. Blue: ERA-Interim in global domain. The curves are plotted for the whole Asia domain.

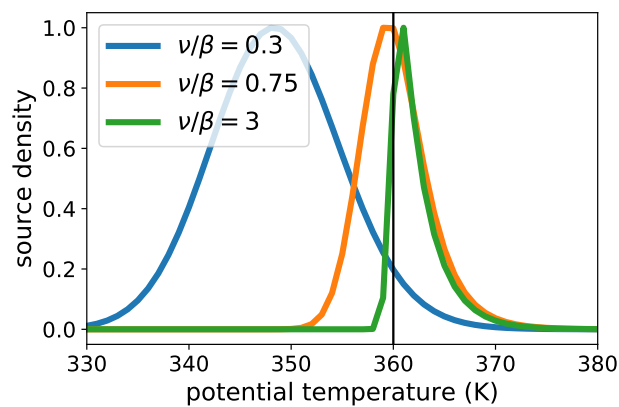


**Figure 14.** Distribution of convective sources according to (2) for  $\theta_0 = 360$  K,  $\beta = 0.4$  K<sup>-1</sup> and three values of  $\nu/\beta$ : 0.3, 0.75 and 3 as indicated in the legend. The proportion of sources above the LZRH  $\theta_0$  in the three cases is, respectively, 4.7%, 55.8% and 97.4%.

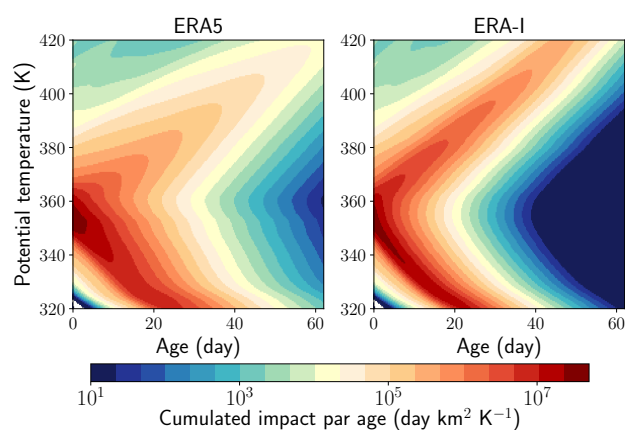


**Figure 15.** Solution of the equation (1) for the observed distribution of high clouds and heating rates within the CoreAMA region defined in Fig. 4. Left panel for ERA5 is to be compared with the upper right panel of Fig. 5. Right panel for ERA-Interim is to be compared with the lower right panel of Fig. 5.

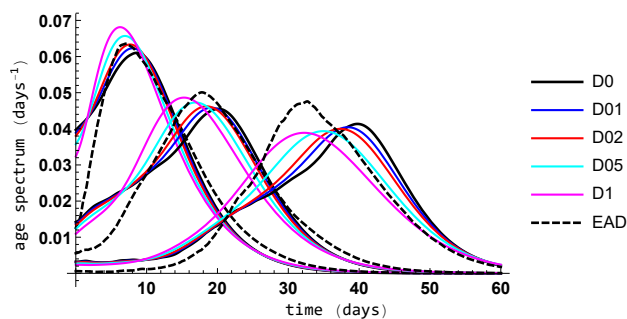


**Figure 16.** Solution of the equation (1) with the same set-up as in Fig. 15 for the diabatic ERA5 case. The normalized age spectrum is shown from left to right at 370 K, 380 K and 400 K for the inviscid solution (D0) and for four values of the diffusion  $K$ :  $0.1 \text{ m}^2\text{s}^{-1}$  (D01),  $0.2 \text{ m}^2\text{s}^{-1}$  (D02),  $0.5 \text{ m}^2\text{s}^{-1}$  (D05) and  $1 \text{ m}^2\text{s}^{-1}$  (D1). The normalized age spectrum for the 3D trajectories (EAD) is shown as a reference.



**Table 1.** Main characteristic numbers for the cloud distribution and the trajectories originating from Asia as a whole and its three sub-regions (Land, Ocean and Tibetan Plateau). When a proportion 100% is in the Asia column, the three other numbers in the row show the contributions of the three regions. EID is not separated into FullAMA and global cases when the distinction does not apply (LZRH and cloud fraction) or when it is negligible (crossover).

		Asia	Land	Ocean	Tibetan Plateau
High clouds SAF	Proportion	100 %	26.6%	68.4%	5.0%
	Max high cloud level	349.5 K	355.5 K	349.5 K	359.5 K
	Mean high cloud level	352.9 K	356.4 K	351.1 K	359.0 K
All sky LZRH	EAD	357.9 K	361.0 K	356.7 K	365.2 K
	EID	352.9 K	357.6 K	351.0 K	366.7 K
Crossover	EAD	363.9 K	364.4 K	362.5 K	364.2 K
	EID	361.7 K	361.8 K	358.5 K	363.1 K
High cloud fraction above crossover	EAD	2.6%	5.1%	1.7%	10.8%
	EID	5.1%	10.4%	4.1%	16.7%
Impact at 380 K and above	EAD FullAMA	100%	54.8%	22.8%	22.4%
	EID FullAMA	100%	54.4%	32.0%	13.6%
	EID global	100%	39.0%	52.9%	8.1%
Mean $\theta$ source for impact at 380 K and above	EAD FullAMA	366.0 K	366.0 K	367.2 K	364.7 K
	EID FullAMA	362.2 K	362.7 K	360.7 K	364.1 K
	EID global	359.2 K	361.5 K	356.7 K	363.7 K
Proportion of source above LZRH for impact at 380 K and above	EAD FullAMA	95.2%	83.5%	95.6%	36.5%
	EID FullAMA	96.5%	87.5%	96.1%	14.2%
	EID global	94.1%	74.1%	81.3%	12.5%